Research Letter

How to Cite: *J. Inorg. Mater.*, 2026, **41(5):** 673
DOI: 10.15541/jim20250442

Anomalous Fluorescence Thermal Quenching in a Red-emitting $RbZnF_3:Eu^{3+}$ Phosphor under Violet Excitation

DONG Langping[1], LI Shixuan[1], YANG Shaoxing[1], HOU Jingshan[1], LIN Yandan[4], ZHOU Pengcheng[5], SUN Xuejiao[3], SUN Yiyang[3], CHEN Daqin[2], FANG Yongzheng[1]

(1. Faculty of Materials Technology, Shanghai Institute of Technology, Shanghai 201418, China; 2. College of Physics and Energy, Fujian Normal University, Fuzhou 350117, China; 3. State Key Laboratory of High Performance Ceramics, Shanghai Institute of Ceramics, Chinese Academy of Sciences, Shanghai 201899, China; 4. College of Intelligent Robotics and Advanced Manufacturing, Fudan University, Shanghai 200438, China; 5. Shanghai Aviation Electric Co., Ltd., Shanghai 201101, China)

Abstract: Thermal quenching is a key challenge in the application of fluorescent materials in solid state lighting devices. Herein, we report a perovskite phosphor $RbZnF_3:Eu^{3+}$ exhibiting anti-thermal quenching behavior. Under violet excitation, this phosphor yields bright red emission. As the temperature rises, the luminescence intensity first increases up to 175 ℃ (*i.e.*, anti-thermal quenching) and then decreases. When the temperature is above 200 ℃, the luminescence intensity falls below the value at room temperature. Comprehensive characterizations demonstrate that the observed anti-thermal quenching behavior is mainly due to the existence of defect levels. First-principles calculations show that Rb vacancy and F vacancy could be responsible for the observed defect levels. Finally, this study has fabricated a white light-emitting diode (LED) using the $RbZnF_3:Eu^{3+}$ phosphor which verifies its potential application.

Key words: phosphor; thermal quenching; perovskite; light-emitting diode; defect engineering

Phosphor-converted white light-emitting diodes (pc-WLEDs) are widely used in daily life due to their environmental protection, low power consumption and long lifetime[1-3]. A typical combination mode of WLED consists of blue LED chip and yellow YAG:Ce^{3+} phosphor[4-8]. The WLED obtained by this method has the problems of poor color reproducibility and high color temperature due to insufficient red light components[9]. To solve the above problems, $CaAlSiN_3:Eu^{2+}$ red phosphor was added in the above-mentioned combination mode to supplement the red light. However, the preparation conditions of $CaAlSiN_3:Eu^{2+}$ nitride phosphor are harsh. Moreover, the Eu^{2+} emission band is broad and extends into the deep red spectral region ($\lambda > 650$ nm), where the eye sensitivity is low[8]. Hence, it is of great importance to exploit new narrow-band red phosphors with mild synthesis conditions. Phosphor is the key component of pc-WLEDs, and its properties directly affect the performance of the devices, especially the thermal stability[9, 10-12]. The heat generated during the operation of WLEDs will make the phosphor thermally quenched, thus affecting the luminous efficiency and white balance of the device[13]. Therefore, phosphors for practical applications are required to have insignificant thermal quenching within specified temperature window.

At present, although some high thermal stability and zero/anti-thermal quenching phosphors have been reported, such as $Na_3Sc_2(PO_4)_3:Eu^{2+}$[2], $K_2BaCa(PO_4)_2:Eu^{2+}$[14], $CsGdGe_3O_9:Eu^{3+}$[7], β-$Al_2O_3:Eu^{2+}$[15], $BaGa_2O_4:Bi^{3+}$[11], $Sr_8ZnSc(PO_4)_7:Tb^{3+}$[16], and $LaAlO_3:Mn^{4+}$[17], almost all of them are prepared by the high-temperature solid phase method. This is primarily because the high-temperature process facilitates the formation of a highly crystalline microstructure with optimized defect structures, which is

Received date: 2025-11-01; **Revised date:** 2025-12-06; **Published online:** 2025-12-19
Foundation item: National Key Research and Development Program of China (2021YFB3500501, 2021YFB3500502, 2021YFB3500503, 2021YFB3500500); National Natural Science Foundation of China (NSFC) (52302188); Shanghai Sailing Program (23YF1446100); Shanghai Rising-Star Program (21QC1401100); Talent Introduction Program of Shanghai Institute of Technology (YJ2022-1)
Biography: DONG Langping (1993–), female, associate professor. E-mail: lpdong@sit.edu.cn
董浪平(1993–), 女, 副教授. E-mail: lpdong@sit.edu.cn
Corresponding author: SUN Yiyang, professor. E-mail: yysun@mail.sic.ac.cn; FANG Yongzheng, professor. E-mail: fyz1003@sina.com
孙宜阳, 研究员. E-mail: yysun@mail.sic.ac.cn; 房永征, 教授. E-mail: fyz1003@sina.com

crucial for achieving excellent thermal stability. However, under low-temperature or room-temperature synthesis routes, restricted atomic diffusion makes it challenging to simultaneously attain high crystallinity and precise defect control. As a result, reports on the preparation of zero/anti-thermal quenching phosphors under such conditions remain scarce. To tackle this issue, the coprecipitation method is quite appealing, which not only can achieve fine and uniform mixing of raw materials, but also exhibits the advantages of simple process, low calcination temperature, short preparation time, and good product performance.

Fluoride perovskite materials with general formula of AMF_3 have been widely studied due to their piezoelectric, magnetic and ion-conductive properties[18]. In this work, we report Eu^{3+}-doped $RbZnF_3$ for the first time. This phosphor can be excited by violet light and shows bright red emission. Interestingly, $RbZnF_3$:Eu^{3+} exhibits excellent thermal stability, where its luminescence intensity increases with the temperature increasing up to 175 ℃, called anti-thermal quenching behavior. We systematically study the mechanism of this intriguing behavior of $RbZnF_3$:Eu^{3+} by a combination of techniques, including first-principles calculations, thermoluminescence, temperature-dependent X-ray diffraction (XRD), X-ray photoelectron spectroscopy (XPS), and electron paramagnetic resonance (EPR). We also fabricated a WLED combining a violet LED chip with the $RbZnF_3$:Eu^{3+} red phosphor, commercial blue and green phosphors demonstrating high performance and great potential of this new phosphor for pc-WLEDs.

1 Experimental

$RbZnF_3$:$x$$Eu^{3+}$ (x%=0.12%–0.17%, in mole) ($RbZnF_3$ is abbreviated as RZF) phosphors were synthesized using the co-precipitation method. The reagent RbF (99%, Titan), $ZnC_4H_6O_4{\cdot}2H_2O$ (99%, Titan) and $Eu(NO_3)_3{\cdot}6H_2O$ (98%, Titan) were utilized as the starting materials. Fig. 1(a) illustrates the process of synthesis. All starting materials were mixed in a molar ratio (Rb+Eu) : Zn : F = 1 : 1 : 3 with methanol, where 3 mmol of RbF (99%) corresponded to 40 mL of methanol. The solution was stirred continuously at room temperature for 6 h until white precipitate appeared. The solution was washed several times repeatedly with absolute ethanol and centrifuged to remove impurities. The precipitate was dried at 60 ℃ for 8–10 h, and the final samples were obtained and then ground into powders for further measurements. The characterization and theoretical calculations details are included in the supporting materials.

2 Results and discussion

2.1 Phase formation and structural analysis

$RbZnF_3$:$x$$Eu^{3+}$ (x%=0.12%–0.17%, in mole) ($RbZnF_3$ is abbreviated as RZF) phosphors were synthesized using the co-precipitation method, as illustrated in Fig. 1(a). Fig. 1(b) presents the XRD patterns of the prepared $RbZnF_3$:$x$$Eu^{3+}$ phosphors. The diffraction peaks of all samples are well matched with those in the standard card, confirming that perovskite phase of $RbZnF_3$ is successfully prepared and the incorporation of Eu^{3+} does not significantly change the phase. $RbZnF_3$ belongs to cubic perovskite structure and the space group is $Pm\bar{3}m$. In the $RbZnF_3$ crystal structure (Fig. 1(c)), one Zn^{2+} coordinates with six F^- to form an octahedron (CN=6, r=0.074 nm), forming a three-dimensional network structure through corner-sharing connections. One Rb^+ coordinates with twelve F^- in the cavities of the network structure (CN=12, r=0.172 nm). Generally, the difference of ion radius between the doped ion and the possibly substituted ion cannot exceed 30%. Here, the ionic radius difference between Eu^{3+} (CN=6, r=0.0947 nm; CN=12, r= 0.152 nm) and Rb^+ is 11%, while that between Eu^{3+} and Zn^{2+} is 28%. This demonstrates that doped Eu^{3+} can occupy both sites but is likely to prefer the Rb^+ sites. It is thus necessary to conduct analysis on the XRD data. If Eu^{3+} occupies a smaller Zn^{2+} site, lattice expansion can be observed and the XRD peaks are expected to shift to smaller angles. If Eu^{3+} occupies a larger Rb^+ site, lattice contraction will be observed and the XRD diffraction peaks will shift to larger angles. According to the zoom-in XRD image (Fig. 1(b)), the main diffraction peak gradually shifts to a large angle with the increased Eu^{3+} concentration, indicating lattice contraction. Thus it is concluded that the Eu^{3+} ions substitute for the Rb^+ ions. This can be further validated in subsequent theoretical calculations.

2.2 Luminescence properties

Fig. 2(a) shows the photoluminescence excitation (PLE) spectrum of $RbZnF_3$:0.13Eu^{3+} detected at 615 nm. The excitation spectrum consists of some narrow excitation bands at 284, 299, 318, 361, 381, 394, 414 and 463 nm, which are generated by $^7F_0\rightarrow{}^5H_3$, $^7F_0\rightarrow{}^5H_4$, $^7F_0\rightarrow{}^5H_6$, $^7F_0\rightarrow{}^5D_4$, $^7F_0\rightarrow{}^5G_{2,4}$, $^7F_0\rightarrow{}^5L_6$, $^7F_0\rightarrow{}^5D_3$ and $^7F_0\rightarrow{}^5D_2$ transitions, respectively[19]. The strongest excitation peak locates at 394 nm, indicating that the synthesized $RbZnF_3$:Eu^{3+} red phosphor can be used for pc-WLED based on violet LED chip. Upon excitation with 394 nm violet light, the photoluminescence (PL) spectrum exhibits dominant emission bands at 592 and 615 nm, along with a distinct peak at around 700 nm,

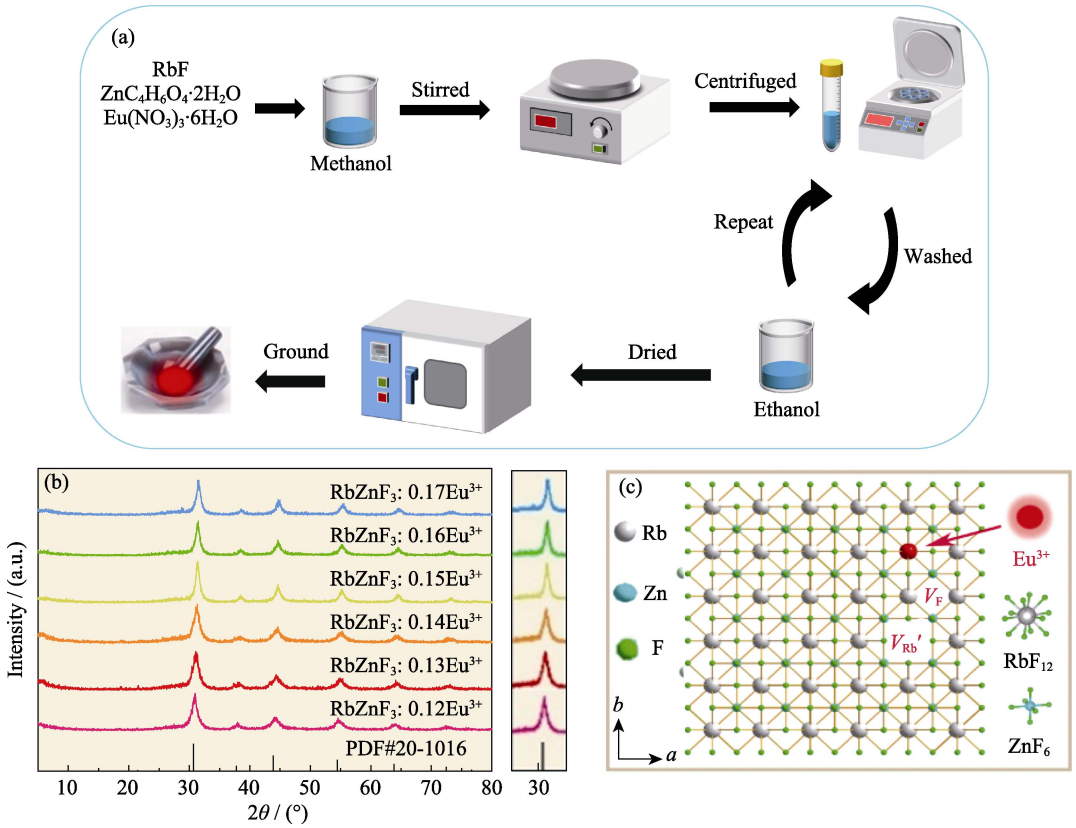

Fig. 1 Synthesis, phase identification and crystal structure of the $RbZnF_3:0.13Eu^{3+}$ phosphor

(a) Schematic diagram of the synthesis process; (b) XRD patterns and enlarged areas at 2θ=25°–35° of the synthesized $RbZnF_3:xEu^{3+}$; (c) Schematic diagram of crystal structure and cation coordination of $RbZnF_3$ matrix

which are assigned to the $^5D_0\rightarrow{}^7F_1$, $^5D_0\rightarrow{}^7F_2$, and $^5D_0\rightarrow{}^7F_4$ transitions of Eu^{3+} ions, respectively (Fig. 2(b))[20-21]. Unlike the weak orange light emission (592 nm) generated by the $^5D_0\rightarrow{}^7F_1$ transition of most existing Eu^{3+} doped luminescent materials, the orange emission of Eu^{3+} activated perovskite structure RZF is comparable to the red emission (615 nm), which is because the doped Eu^{3+} is located in a highly symmetric environment[7].

To optimize the luminescence performance of Eu^{3+} in the $RbZnF_3$ matrix, a series of $RbZnF_3:xEu^{3+}$ phosphors were prepared and their emission spectra were collected, as shown in Fig. 2(c). When the concentration of Eu^{3+} is 0.13%, the luminescence intensity of the sample reaches the highest value (Fig. 2(d)). With further increasing of Eu^{3+} doping content, the PL intensity of $RbZnF_3:xEu^{3+}$ decreases continuously due to the enhanced non-radiative energy transfer between the Eu^{3+} ions. Energy transfer is usually conducted through the exchange and electric multipolar interactions. Exchange interaction is only effective when the critical distance is smaller than 0.5 nm. To determine the energy transfer mechanism of Eu^{3+} in the $RbZnF_3$ matrix, it is necessary to calculate the critical distance (R_C) by the following formula[22]:

$$R_C = 2\left(\frac{3V}{4\pi x_C N}\right)^{\frac{1}{3}} \quad (1)$$

where the unit cell volume V is 0.0705935 nm^3, the critical concentration x_C is 0.13, and the number of occupied cations N is 1. The critical distance R_C is determined to be 1.1 nm, greater than 0.5 nm, so the energy transfer between the Eu^{3+} ions is expected to be dominated by the electric multipolar interaction. The specific type of electric multipolar interaction can be determined by the following formula[23-24]:

$$\lg\left(\frac{I}{x}\right) = -\frac{s}{3}\lg x + \lg f \quad (2)$$

where x represents the doping concentration of Eu^{3+}, I represents the luminous intensity, f is a constant independent of concentration, and s denotes the interaction type: 6 (dipole-dipole), 8 (dipole-quadrupole), or 10 (quadrupole-quadrupole). The relationship between $\lg(I/x)$ and $\lg x$ is shown in Fig. S1. The slope of the linear fitting ($-s/3$) is about –1.95, that is, s is closer to 6, indicating that the energy transfer mechanism of Eu^{3+} in the $RbZnF_3$ matrix is dominated by dipole-dipole interaction.

The luminescence kinetics of Eu^{3+} in the $RbZnF_3$ matrix was also studied. The decay curve of $RbZnF_3:0.13Eu^{3+}$ at 615 nm under 394 nm excitation is shown in Fig. S2. The decay curve can be well fitted by a single exponential decay[14]:

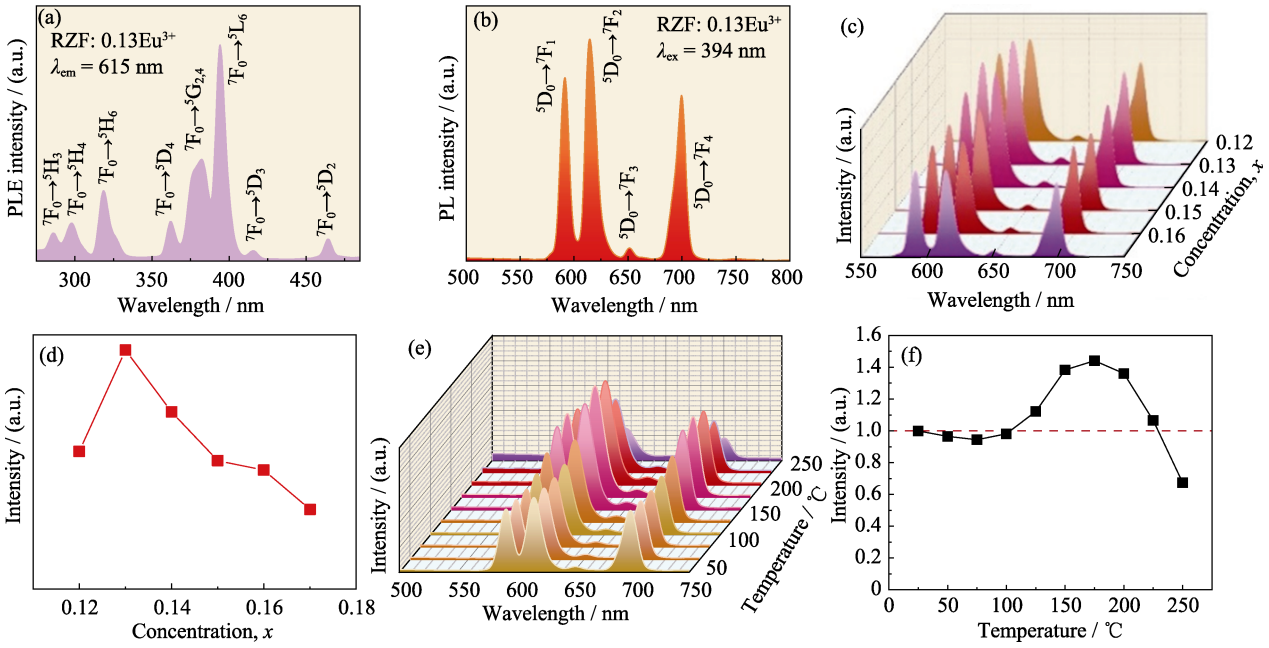

Fig. 2 Photoluminescence, concentration quenching and thermal quenching behavior of $RbZnF_3$:0.13Eu^{3+} (a) Excitation and (b) emission spectra of $RbZnF_3$:0.13Eu^{3+}; (c) Emission spectra of $RbZnF_3$:$x$$Eu^{3+}$ samples; (d) Relationship between concentration x and luminescence intensity; (e) Temperature-dependent emission spectra of $RbZnF_3$:0.13Eu^{3+} sample; (f) Evolution trend of luminescence intensity with increasing temperature

$$I(t) = I_0 + A_1\left(\frac{-t}{\tau_1}\right) \quad (3)$$

where $I(t)$ is the luminescence intensity at a given time t after excitation ceases. The constant I_0 accounts for the background signal, while A_1 is the amplitude. The key parameter τ_1 is the decay lifetime, characterizing the time required for the intensity to decrease to 1/e of its initial value. The decay lifetime of Eu^{3+} was determined to be 1.18 ms, which is of the same order of magnitude as the reported lifetime. The single-exponential decay curve further proves that Eu^{3+} occupies a single site in the RZF matrix.

2.3 Fluorescence thermal stability

Fig. 2(e) shows the temperature-dependent emission spectra of the $RbZnF_3$:0.13Eu^{3+} sample. Surprisingly, when the temperature was increased from 25 to 100 ℃, the luminescent intensity of the $RbZnF_3$:0.13Eu^{3+} sample did not decay significantly. When the temperature increases from 25 to 100 ℃, a slight decrease in luminescence intensity is observed in the initial heating stage. This can be attributed to the enhancement of phonon-assisted non-radiative transitions at relatively low temperatures. Increased lattice vibrations (phonons) provide additional pathways for the excited Eu^{3+} ions to relax non-radiatively, dissipating part of their energy as heat, which leads to a slight reduction in luminescence efficiency. This represents the onset of the conventional thermal quenching behavior common to most phosphors[25-26]. Surprisingly, with the further increase of temperature, the luminescent intensity of $RbZnF_3$:0.13Eu^{3+} phosphor increases continuously until 175 ℃ (Fig. 2(f)), indicating anti-thermal quenching behavior, which is greatly beneficial to its application in WLED. When the temperature is above 200 ℃, the luminescence intensity falls below the value at room temperature. Additionally, repeated thermal-quenching measurements were performed on the $RbZnF_3$:0.13Eu^{3+} phosphor (the corresponding results are shown in Fig. S3). The results reproduce the trend observed in the previous test, confirming the reproducibility of the anomalous thermal-quenching behavior of $RbZnF_3$:Eu^{3+}. Several mechanisms have been proposed regarding zero/anti-thermal quenching mechanisms, including negative thermal expansion crystal structures, phase transitions, and crystal defects[10, 27]. To analyze the cause of the anti-thermal quenching phenomenon in order to guide the design and synthesis of phosphors with high thermal stability, the mechanism of anti-thermal quenching of $RbZnF_3$:0.13Eu^{3+} was systematically studied.

Firstly, the rigidity of crystal structure is studied. Good crystal structure rigidity is regarded as an ideal indicator of high thermal stability. Debye temperature (Θ_D) is positively correlated with the rigidity, and its function can be described as follows[28]:

$$\Theta_D = \frac{\hbar}{k_B}\left(6\pi^2 V^{\frac{1}{2}} n\right)^{\frac{1}{3}}\left\{3\left[2\left(\frac{2}{3}\cdot\frac{1+\sigma}{1-2\sigma}\right)^{\frac{3}{2}}+\left(\frac{1}{3}\cdot\frac{1+\sigma}{1-\sigma}\right)^{\frac{3}{2}}\right]^{-1}\right\}^{\frac{1}{3}}\sqrt{\frac{B_s}{M}} \quad (4)$$

where $\hbar$ represents the Plank constant, k_B represents the Boltzmann constant, V is the unit cell volume, n represents the number of formula units in the unit cell, σ represents the Poisson's ratio, B_s represents the adiabatic bulk modulus, and M represents the average mass per formula unit. For $RbZnF_3$:0.13Eu^{3+}, the parameters used in the calculation are as follows: the unit cell volume (V= 0.0705935 nm^3) was obtained from Rietveld refinement of the XRD data; the Poisson's ratio (σ=0.278) and adiabatic bulk modulus (B_s=69.2 GPa) were adopted from first-principles calculations; the unit cell mass (M= 36.1 g/mol) was calculated based on the chemical stoichiometry. Based on these values, the Debye temperature of $RbZnF_3$:0.13Eu^{3+} is calculated to be 309 K. Compared with existing rigid structural materials ($BaSr_2SiO_5$:1%Eu^{2+}, Θ_D=525 K[29]; Y_2SiO_5:Ce^{3+}, Θ_D= 512 K[28]; $Sr_3(PO_4)_2$:Eu^{2+}, Θ_D=559 K[30]; $Y_3Al_5O_{12}$, Θ_D= 726 K[31]), it can be concluded that structure rigidity is not the dominant factor for the anti-thermal quenching of $RbZnF_3$:0.13Eu^{3+}.

Fig. 3(a) presents temperature-dependent XRD patterns of $RbZnF_3$:0.13Eu^{3+} sample. When the temperature increases from 25 to 175 ℃, the $RbZnF_3$:0.13Eu^{3+} sample remains pure phase, indicating its good thermal stability and excluding the phase transition mechanism of supplementary heat loss. To further obtain the structural information at different temperatures, Rietveld structure refinements of the Eu^{3+}-doped $RbZnF_3$ sample at different

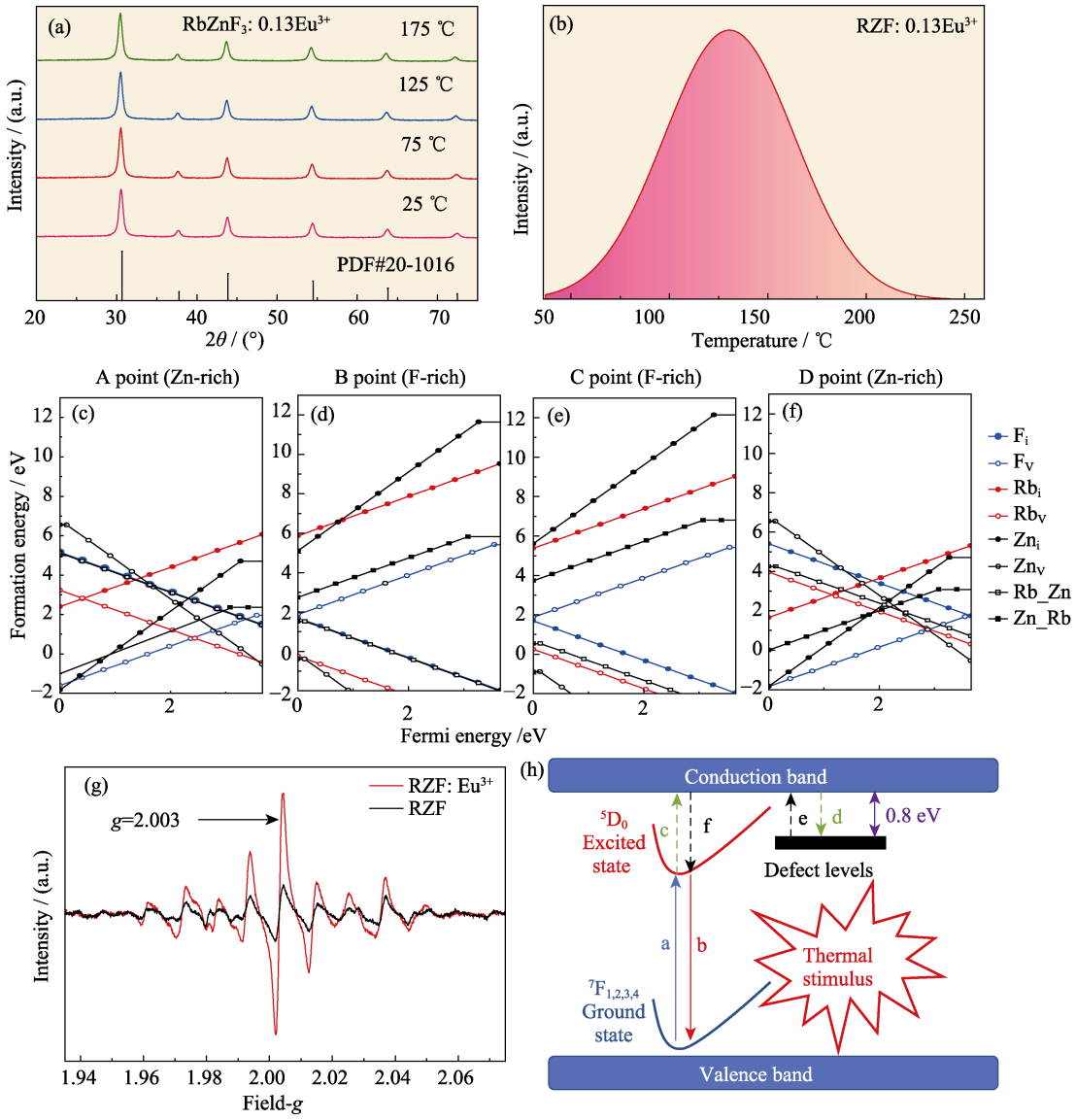

Fig. 3 Investigation of the anti-thermal quenching performance and mechanism in $RbZnF_3$:0.13Eu^{3+} phosphor

(a) Temperature-dependent XRD patterns of $RbZnF_3$:0.13Eu^{3+} sample; (b) Thermoluminescence curve of $RbZnF_3$:0.13Eu^{3+} sample at different temperatures; (c-f) Defect forming energy of various defects when the chemical composition is (c) A, (b) B, (c) C, and (d) D points; (g) EPR spectra for RZF and RZF:Eu^{3+}; (h) Schematic illustration of the mechanism for the anti-thermal quenching in RZF:0.13Eu^{3+} phosphor. Colorful figures are available on website

temperatures were carried out. The Rietveld refinement patterns of $RbZnF_3$:0.13Eu^{3+} sample at different temperatures (25–175 ℃) are shown in Fig. S4. The observed results are highly matched with the calculated results, further demonstrating the high phase and structural stability of the prepared samples. In addition, the cell parameter *a* and cell volume *V* tend to expand slightly with the temperature increasing from 25 to 175 ℃ (Table S1), so the anti-thermal quenching cannot be attributed to the negative thermal expansion structure.

Another reason for anti-thermal quenching is the presence of defects. Defects in the crystal structure can capture electrons, which can be released at high temperatures. This process can maintain the luminescence intensity at high temperatures and improve the thermal stability of phosphors. When trivalent Eu^{3+} substitute Rb^+ ions, there are two possible ways to maintain the electrical neutrality of the crystal. The first way is that one Eu^{3+} ion replaces three Rb^+ ions to produce two negatively charged V'_{Rb} vacancy defects and one $[Eu^{3+}]^{\bullet\bullet}_{Rb}$ defect with two positive charges, the defect reaction equation is as follows:

$$3Rb^+ \rightarrow [Eu^{3+}]^{\bullet\bullet}_{Rb} + 2V'_{Rb} \quad (5)$$

The second way is to introduce F^- interstitial ions (F'_i), which can be described by as the following equation:

$$Rb^+ \rightarrow [Eu^{3+}]^{\bullet\bullet}_{Rb} + 2F'_i \quad (6)$$

It is conducted that theoretical calculations on the formation energy of possible defects in several specific compositions to determine which type of defect is more likely to be present. Figs. 3(c-f) show the calculated defect formation energy for possible intrinsic defects at different chemical potentials (Fig. S5), where F_i and Rb_i represent F^- and Rb^+ interstitial ions, respectively, and V_F and V_{Rb} represent F^- and Rb^+ vacancies, respectively. From the calculation results, it can be seen that regardless of the chemical potentials, the formation energy of Rb^+ vacancies is always lower than that of F^- interstitials, indicating that Rb^+ vacancy defects are more likely to form.

Furthermore, to investigate whether defect induced anti-thermal quenching behavior is universal, Tb^{3+} doped RZF was synthesized and its temperature-dependent luminescence properties were studied. The temperature-dependent emission spectra of RZF:Tb^{3+} under 378 nm excitation were collected and presented in Fig. S6(a). With the temperature increasing, the PL intensity of RZF:Tb^{3+} shows a slight decrease and then increases (Fig. S6(b)), showing a similar trend to that of Eu^{3+} doped samples. This result indicates that the anti-thermal quenching behavior introduced by defects holds certain universality in the RZF matrix.

Thermoluminescence is an effective technique for studying various aspects of defects in phosphor materials. Fig. 3(b) presents the thermoluminescence curve of $RbZnF_3$:0.13Eu^{3+} sample. With the increase of temperature, the thermoluminescence of the defect level enhances. The fastest release is at 125 ℃, after which the energy release gradually slows down. The depth of the trap can be estimated by the following equation[2, 17]:

$$E_T = T_M/500 \quad (7)$$

where E_T (eV) represents the thermal activation energy of trap depth, and T_M (K) is the temperature corresponding to the peak value of the thermoluminescence spectrum. For the prepared $RbZnF_3$:0.13Eu^{3+} sample, the thermal activation energy of the trap is calculated to be 0.8 eV. The thermoluminescence spectrum results confirm the formation of the defect and the contribution of the defect to thermal stability, which could explain the anti-thermal quenching behavior when increasing temperature above 100 ℃.

In addition to the cation vacancy V'_{Rb} mentioned above, intrinsic defects, such as F^- vacancy, may be formed during the preparation of materials. The thermoluminescence curve of $RbZnF_3$ matrix at different temperatures was collected and displayed in Fig. S7. As the temperature elevates, the thermoluminescence increases, indicating the possible presence of intrinsic defects in the RZF matrix. EPR is a technique to characterize defects. As shown in Fig. 3(g) for the EPR data of Eu^{3+} doped and undoped samples, an EPR signal at g=2.003 is observed in the sample of $RbZnF_3$:Eu^{3+}, which could be assigned to the F vacancies[32]. This result suggests that the anti-thermal quenching is possibly caused by the synergistic effect of Rb^+ vacancy and F^- vacancy defects.

The mechanism of the anti-thermal quenching behavior of $RbZnF_3$:Eu^{3+} caused by defect energy level can be described using the simplified schematic model shown in Fig. 3(h). When excited by light, the electrons of Eu^{3+} transition from the ground state $^7F_{1,2,3,4}$ to the excited state $^5D_0$ (path a). Then, some electrons return to the ground state by a radiative process (path b), generating red light emission. In the presence of defect levels, some electrons in the excited state $^5D_0$ can enter the conduction band of the host crystal (path c) under thermal ionization and be trapped by the defect levels (path d). When the phosphor is heated to a specific critical temperature, the electrons in the defect level are released under thermal stimulation entering the conduction band of the host crystal (path e). Then, the electrons

recombine with the $^5D_0$ level (path f) and return to the ground state $^7F_{1,2,3,4}$ (path b) through luminescence. This process above compensates for the luminescence intensity at high temperatures giving rise to anti-thermal quenching behavior.

2.4 LED application

Finally, a WLED was fabricated by combining violet LED chip with $BaMgAl_{10}O_{17}:Eu^{2+}$ (BAM:Eu^{2+}, λ_{em}=450 nm) blue phosphor, $(Ba, Sr)_2SiO_4:Eu^{2+}$ (λ_{em}=505 nm) green phosphor and the prepared RZF:0.13Eu^{3+} red phosphor in a ratio of 1 : 2 : 2. The BAM:Eu^{2+} and $(Ba, Sr)_2SiO_4:Eu^{2+}$ phosphors were purchased from Ningbo MPRO Materials Co., Ltd. The electroluminescence (EL) spectrum of the manufactured WLED is shown in Fig. 4. The correlated color temperature (CCT), color rendering index (Ra), and CIE chromaticity coordinates were measured using an Everfine YF1000 measurement system equipped with an integrating sphere. The fabricated WLED emits warm white light (inset in Fig. 4) with a low CCT of 5336 K, a high Ra of 85.9 and a CIE of (0.3389, 0.3462), which reveals the application potential of the prepared $RbZnF_3:Eu^{3+}$ red phosphor in WLED.

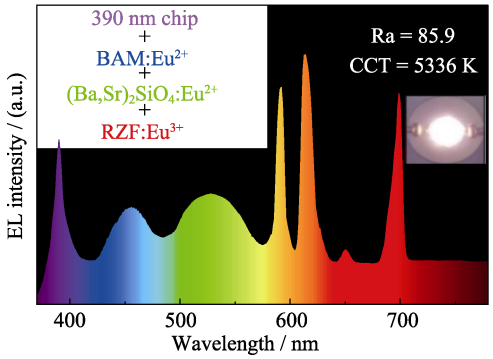

Fig. 4 Electroluminescence spectrum of WLED produced by 390 nm violet LED chip combining BAM:Eu^{2+} blue phosphor, $(Ba, Sr)_2SiO_4:Eu^{2+}$ green phosphor and prepared RZF:0.13Eu^{3+} red phosphor
Inset: a photo of the fabricated WLED when it is powered on

3 Conclusions

A thermally stable red phosphor $RbZnF_3:Eu^{3+}$ with perovskite structure was prepared at room temperature for the first time. Its structure, composition, luminescent properties were systematically studied. When monitoring 615 nm emission, the excitation spectrum features several narrow bands with the strongest peak occurring at 394 nm, which is well matched with commercially available violet LED chips. When stimulated by 394 nm violet light, $RbZnF_3:Eu^{3+}$ emits strong red light. Owing to high structural symmetry, the orange emission band at 592 nm is comparable to the red emission band at 615 nm in the spectrum. As temperature increases, the luminescence intensity of $RbZnF_3:Eu^{3+}$ anomalously increases until about 175 ℃. Combined first-principles calculations and thermoluminescence analysis show that intrinsic defects account for the anti-thermal quenching behavior of $RbZnF_3:Eu^{3+}$. A fabricated WLED using $RbZnF_3:Eu^{3+}$ as the red phosphor exhibits a low CCT of 5336 K, a high Ra of 85.9 and a CIE of (0.3389, 0.3462), which suggests that $RbZnF_3:Eu^{3+}$ could be a potential red emitter for violet-LED-chip-excited WLED.

Supporting Materials

Supporting materials related to this article can be found at https://doi.org/10.15541/jim20250442.

References:

[1] ZHONG C, XU Y, WU X, *et al*. High output power and high quantum efficiency in novel NIR phosphor $MgAlGa_{0.7}B_{0.3}O_4:Cr^{3+}$ with profound FWHM variation. *Advanced Materials*, 2024, **36:** 2309500.

[2] KIM Y H, ARUNKUMAR P, KIM B Y, *et al*. A zero-thermal-quenching phosphor. *Nature Materials*, 2017, **16:** 543.

[3] YUAN W, PANG R, WANG S, *et al*. Enhanced blue-light excited cyan-emitting persistent luminescence of $BaLu_2Al_2Ga_2SiO_{12}:Ce^{3+}$, Bi^{3+} phosphors for AC-LEDs *via* defect modulation. *Light: Science & Applications*, 2022, **11:** 184.

[4] DONG L, ZHANG L, JIA Y, *et al*. Enhancing luminescence and controlling the Mn valence state of $Gd_3Ga_{5-x-\delta}Al_{x-y+\delta}O_{12}:y$Mn phosphors by the design of the garnet structure. *ACS Applied Materials & Interfaces*, 2020, **12:** 7334.

[5] DONG L, ZHANG L, JIA Y, *et al*. Site occupation and luminescence of novel orange-red $Ca_3M_2Ge_3O_{12}:Mn^{2+}$, Mn^{4+} (M = Al, Ga) phosphors. *ACS Sustainable Chemistry & Engineering*, 2020, **8:** 3357.

[6] PAN X, MEI L, ZHUANG Y, *et al*. Anti-defect engineering toward high luminescent efficiency in whitlockite phosphors. *Chemical Engineering Journal*, 2022, **434:** 134652.

[7] DANG P, LI G, YUN X, *et al*. Thermally stable and highly efficient red-emitting Eu^{3+}-doped $Cs_3GdGe_3O_9$ phosphors for WLEDs: non-concentration quenching and negative thermal expansion. *Light: Science & Applications*, 2021, **10:** 29.

[8] SENDEN T, VAN DIJK-MOES R J A, MEIJERINK A. Quenching of the red Mn^{4+} luminescence in Mn^{4+}-doped fluoride LED phosphors. *Light: Science & Applications*, 2018, **7:** 8.

[9] WEI Y, XING G, LIU K, *et al*. New strategy for designing orangish-red-emitting phosphor *via* oxygen-vacancy-induced electronic localization. *Light: Science & Applications*, 2019, **8:** 15.

[10] DANG P, WANG W, LIAN H, *et al*. How to obtain anti-thermal-quenching inorganic luminescent materials for light-emitting diode applications. *Advanced Optical Materials*, 2022, **10:** 2102287.

[11] LI H, CAI J, PANG R, *et al*. A strategy for developing thermal-quenching-resistant emission and super-long persistent luminescence in $BaGa_2O_4:Bi^{3+}$. *Journal of Materials Chemistry C*, 2019, **7:** 13088.

[12] WEI S, LYU Z, LU Z, *et al*. Moderate trap engineering for

enhanced thermal stability and high efficiency in a Bi^{3+}-doped phosphor. *Chemistry of Materials*, 2023, **35:** 7125.
[13] DAI P P, LI C, ZHANG X T, *et al*. A single Eu^{2+}-activated high-color-rendering oxychloride white-light phosphor for white-light-emitting diodes. *Light: Science & Applications*, 2016, **5:** e16024.
[14] QIAO J, NING L, MOLOKEEV M S, *et al*. Eu^{2+} site preferences in the mixed cation $K_2BaCa(PO_4)_2$ and thermally stable luminescence. *Journal of the American Chemical Society*, 2018, **140:** 9730.
[15] PIAO S, WANG Y, ZHOU X, *et al*. Defect engineering in a Eu^{2+}-doped β-Al_2O_3 structure blue phosphor and its controllable zero-thermal quenching luminescence. *ACS Sustainable Chemistry & Engineering*, 2021, **9:** 7882.
[16] CHEN Y, YU B, GOU J, *et al*. Zero-thermal-quenching and photo-luminescence tuning with the assistance of carriers from defect cluster traps. *Journal of Materials Chemistry C*, 2018, **6:** 10687.
[17] FANG S, LANG T, HAN T, *et al*. Zero-thermal-quenching of Mn^{4+} far-red-emitting in $LaAlO_3$ perovskite phosphor *via* energy compensation of electrons' traps. *Chemical Engineering Journal*, 2020, **389:** 124297.
[18] TYAGI N, KUMAR P S, NAGARAJAN R. Room temperature optical absorption and intrinsic photoluminescence in $KZnF_3$. *Chemical Physics Letters*, 2010, **494:** 284.
[19] WEI S, LI Z, LYU Z, *et al*. Energy transfer mediated single-phased white light emission in Bi^{3+}-Eu^{3+} codoped $Ba_3YGa_2O_{7.5}$ for WLED. *Journal of Alloys and Compounds*, 2022, **923:** 166419.
[20] AN Z, LIU W, SONG Y, *et al*. Color-tunable Eu^{2+}, Eu^{3+} co-doped $Ca_{20}Al_{26}Mg_3Si_3O_{68}$ phosphor for w-LEDs. *Journal of Materials Chemistry C*, 2019, **7:** 6978.
[21] LI R, CHEN Q, CUI R, *et al*. A novel high-brightness red phosphor $Ca_4Nb_2O_9$:Eu^{3+} for WLEDs. *Inorganic Chemistry Communications*, 2024, **170:** 113267.
[22] BLASSE G. Energy transfer in oxidic phosphors. *Physics Letters A*, 1968, **28:** 444.
[23] TIAN Y, CHEN B, TIAN B, *et al*. Concentration-dependent luminescence and energy transfer of flower-like $Y_2(MoO_4)_3$:Dy^{3+} phosphor. *Journal of Alloys and Compounds*, 2011, **509:** 6096.
[24] HUANG S, LOU L. Concentration dependence of sensitizer fluorescence intensity in energy transfer. *Chinese Journal of Luminescence*, 1990, **11:** 1.
[25] LI J, LIU B, LIU G, *et al*. Red color $Sr_2NaMg_2V_3O_{12}$:Eu^{3+} phosphor with high thermal stability for w-LEDs. *Journal of Rare Earths*, 2023, **41:** 1689.
[26] LI F, CUI R, YUAN G, *et al*. Preparation and characterization of a new orange-red phosphor Ba_2LaTaO_6:Eu^{3+} with abnormal thermal quenching. *Journal of Rare Earths*, 2023, **41:** 1678.
[27] BAI Y, JIA Z, GAO J, *et al*. A novel red-emitting phosphor K_2MgGeO_4:Eu^{3+} for WLEDs: zero-thermal quenching induced by heterovalent substitution. *Journal of Materials Chemistry C*, 2022, **10:** 15957.
[28] HA J, WANG Z, NOVITSKAYA E, *et al*. An integrated first principles and experimental investigation of the relationship between structural rigidity and quantum efficiency in phosphors for solid state lighting. *Journal of Luminescence*, 2016, **179:** 297.
[29] LIU H, LIANG H, ZHANG W, *et al*. Improving the thermal stability and luminescent efficiency of $(Ba,Sr)_3SiO_5$:Eu^{2+} phosphors by structure, bandgap engineering and soft chemistry synthesis method. *Chemical Engineering Journal*, 2021, **410:** 128367.
[30] SUN Z, SUN B, ZHANG X, *et al*. Superb thermal stability purple-blue phosphor through synergistic effect of emission compensation and nonradiative transition restriction of Eu^{2+}. *Materials Today Chemistry*, 2022, **24:** 100877.
[31] WANG Z, JIAO S, XU Y, *et al*. Effects of heat-treatment on photoluminescence properties of $MgAl_2O_4$:Eu^{3+} red phosphors synthesized by a solution combustion method. *Journal of Luminescence*, 2019, **211:** 108.
[32] LI X, HE C, ZUO S, *et al*. Photocatalytic nitrogen fixation over fluoride/attapulgite nanocomposite: effect of upconversion and fluorine vacancy. *Solar Energy*, 2019, **191:** 251.

一种可被紫光激发的红色荧光粉 $RbZnF_3$:Eu^{3+} 中的异常热猝灭现象

董浪平[1], 李施璇[1], 杨少星[1], 侯京山[1], 林燕丹[4], 周鹏程[5], 孙雪娇[3], 孙宜阳[3], 陈大钦[2], 房永征[1]

(1. 上海应用技术大学 材料技术学部, 上海 201418; 2. 福建师范大学 物理与能源学院, 福州 350117; 3. 中国科学院 上海硅酸盐研究所, 关键陶瓷材料全国重点实验室, 上海 201899; 4. 复旦大学 智能机器人及先进制造创新学院, 上海 200438; 5. 上海航空电器有限公司, 上海 201101)

摘 要: 热猝灭是荧光材料在固态照明器件中应用时面临的关键挑战。本研究报道了一种具有抗热猝灭行为的钙钛矿型荧光粉 $RbZnF_3$:Eu^{3+}。在紫光激发下, 该荧光粉发出明亮的红光。随着温度升高, 其发光强度先增大(175 ℃, 即抗热猝灭), 随后下降; 当温度高于 200 ℃时, 发光强度低于室温值。通过全面表征发现, 抗热猝灭行为主要源于缺陷能级的存在。第一性原理计算表明, Rb 空位和 F 空位可能是形成这些缺陷能级的主要原因。本研究还利用 $RbZnF_3$:Eu^{3+}荧光粉制备了白光发光二极管(LED), 验证了其潜在应用价值。

关 键 词: 荧光粉; 热猝灭; 钙钛矿; 发光二极管; 缺陷工程

中图分类号: TB34 **文献标志码:** A **文章编号:** 1000-324X(2026)05-0673-08

Supporting Information:

Anomalous Fluorescence Thermal Quenching in a Red-emitting $RbZnF_3:Eu^{3+}$ Phosphor under Violet Excitation

DONG Langping[1], LI Shixuan[1], YANG Shaoxing[1], HOU Jingshan[1], LIN Yandan[4], ZHOU Pengcheng[5], SUN Xuejiao[3], SUN Yiyang[3], CHEN Daqin[2], FANG Yongzheng[1]

(1. Faculty of Materials Technology, Shanghai Institute of Technology, Shanghai 201418, China; 2. College of Physics and Energy, Fujian Normal University, Fuzhou 350117, China; 3. State Key Laboratory of High Performance Ceramics, Shanghai Institute of Ceramics, Chinese Academy of Sciences, Shanghai 201899, China; 4. College of Intelligent Robotics and Advanced Manufacturing, Fudan University, Shanghai 200438, China; 5. Shanghai Aviation Electric Co., Ltd., Shanghai 201101, China)

S1 Characterization

X-ray diffraction (XRD) data was collected by Bruker D8 Focus diffractometer with Cu Kα radiation. The morphology and elemental mapping analysis were examined by scanning electron microscope (SEM, JEOL JSM-6510). The diffuse reflectance spectra were collected with a Hitachi U-4100 UV-vis-NIR spectrophotometer. The photoluminescence excitation (PLE) and emission (PL) spectra were characterized using a Hitachi F-7000 fluorescence spectrometer (Tokyo, Japan) equipped with a 150 W xenon lamp as an excitation source. The decay curve was recorded using a steady state and transient state fluorescence spectrometer (FS5, Edinburgh). Temperature-dependent PL spectra were collected using a fluorescence spectrophotometer (Edinburgh Instruments FLSP-920) with a temperature controller. Temperature-dependent XRD data were also recorded on a D8 Advance X-ray diffractometer with a temperature controller. Thermoluminescence (TL) spectra were measured using a homemade instrument equipped with a heating apparatus and a CCD detector. X-ray photoelectron spectroscopy (XPS) measurements were carried out on the Thermo SCIENTIFIC ESCALAB 250Xi with an Al Kα source. Electron paramagnetic resonance (EPR) spectra were measured by using a Bruker E580 EPR spectrometer operating at the X-band microwave frequency. Raman spectra were recorded by using a DXR-Raman spectrometer with 532 nm laser line.

S2 Theoretical calculations

First-principles calculations were based on density functional theory (DFT), as implemented in the Vienna *ab initio* Simulation Package (VASP)[S1]. The interaction between ion-cores and valence electrons was described by the projector augmented-wave (PAW) method. The cutoff energy for the plane-wave basis was set to 400 eV. The exchange-correlation energy is treated using the Perdew-Burke-Ernzerhof for solids (PBEsol) functional. Defect models are constructed using the supercell approach, with the perfect supercell containing 320 atoms. The Brillouin zone of the defect supercell is sampled by the Γ point. All calculations are performed with spin polarization. During structural relaxation, the atomic positions are fully relaxed until the residual forces on all atoms are smaller than 0.025 eV/Å. The defect formation energy is a function of atomic chemical potentials and the Fermi level. For a point defect with charge state q, the formation energy can be expressed as[S2-S3]:

$$\Delta \boldsymbol{H}(\{\mu_i\}, E_{\mathrm{F}}, q) = E_{\mathrm{D}}^{q} - E_{\mathrm{P}} + \sum_i n_i(\mu_i^* + E_i) + q(E_{\mathrm{F}} + E_{\mathrm{VBM}}) \quad \text{(S1)}$$

Here, E_{D}^{q} is the total energy of the supercell containing a defect with charge q, E_{P} is the total energy of the perfect crystal, and n_i represents the number of atoms of species i added ($n_i < 0$) or removed ($n_i > 0$) during defect formation. μ_i^* is the chemical potential of element i, and E_i is the total energy per atom in its stable phase. The allowable range of μ_i^*, as shown in Fig. S7, is determined by the possible secondary phases. E_{VBM} is the valence-band maximum (VBM) energy of the host material, and E_F is the Fermi level, which varies between the VBM and the conduction-band minimum (CBM). When calculating charged defects, a uniform compensating background charge is assumed to maintain overall charge neutrality in the supercell.

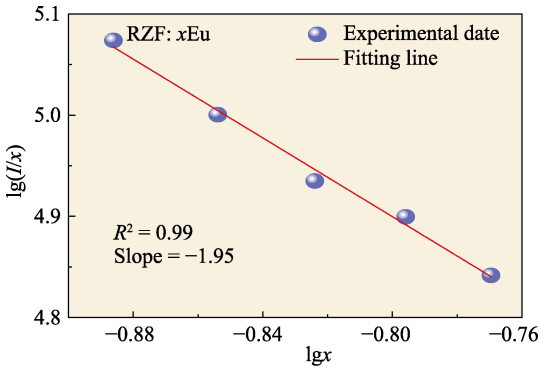

Fig. S1 Relationship of lg(*I*/*x*) *versus* lg*x*

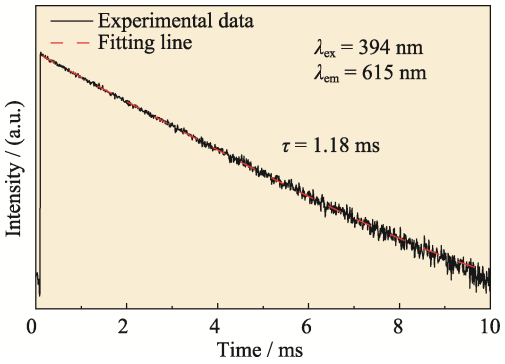

Fig. S2 Decay curve of $RbZnF_3$:0.13Eu^{3+}

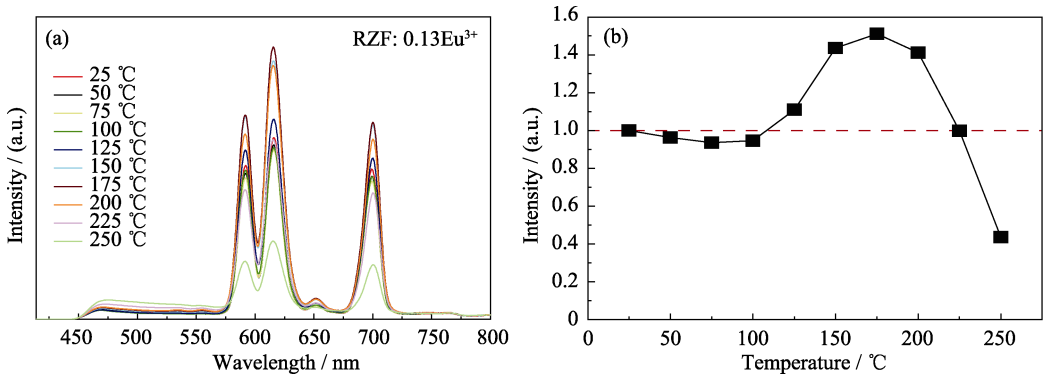

Fig. S3 Repeated testing of the thermal quenching process in $RbZnF_3$:0.13Eu^{3+}
(a) Thermal-dependent emission spectra of $RbZnF_3$:0.13Eu^{3+}; (b) Evolution of the luminescence intensity as a function of temperature during repeated testing

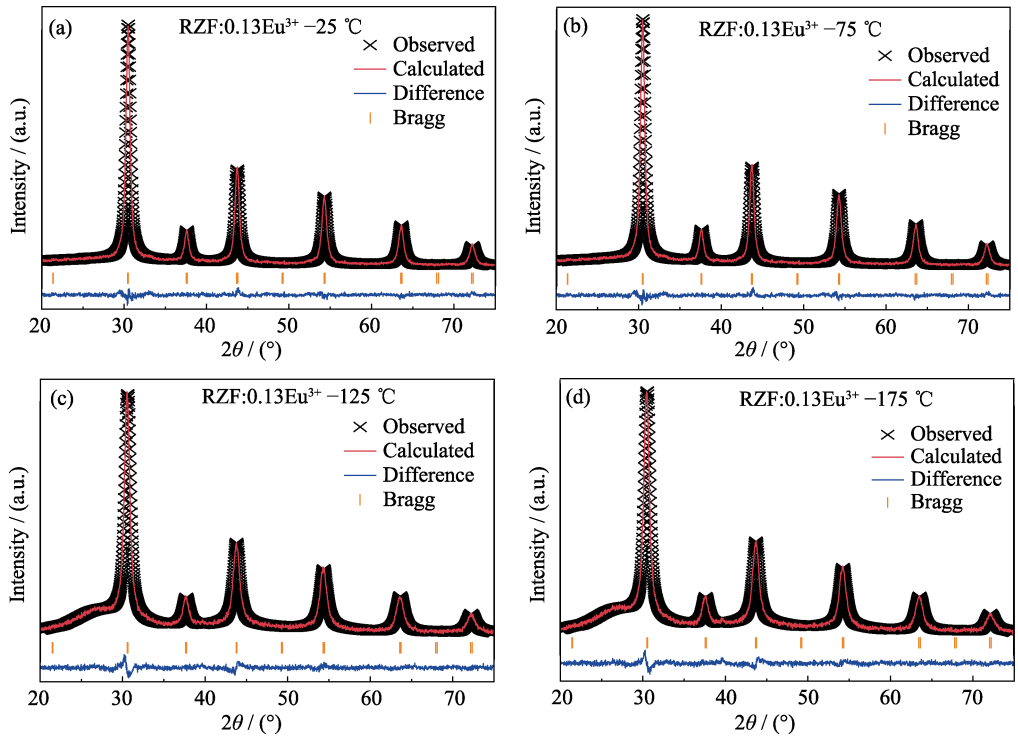

Fig. S4 Rietveld refinement patterns of $RbZnF_3$:0.13Eu^{3+} sample at different temperatures

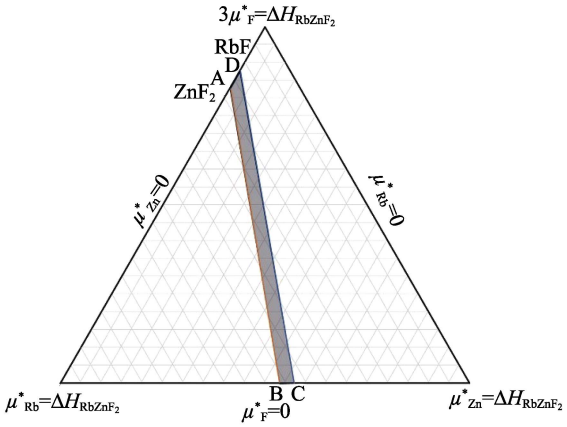

Fig. S5 Chemical potential and potential chemical composition distribution

A and D are extreme composition points rich in Zn, while B and C are extreme composition points rich in F. $RbZnF_3$ can only form within a closed area composed of points A, B, C, and D

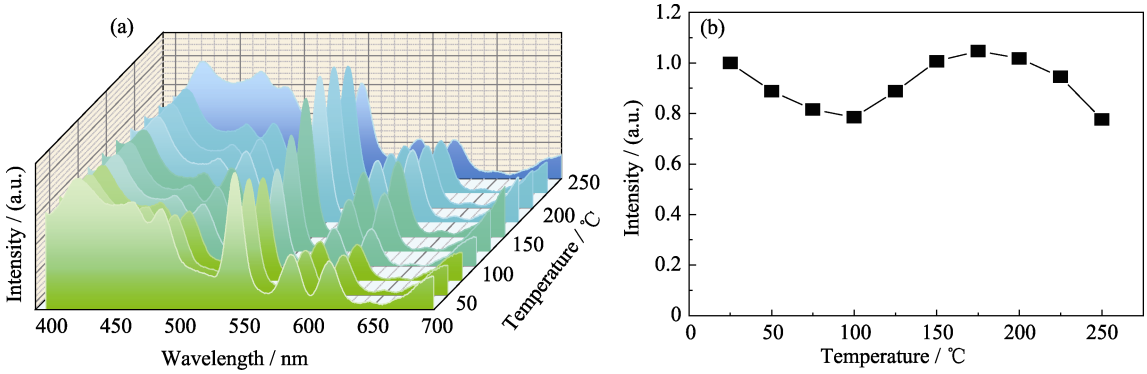

Fig. S6 Evaluation of the thermal quenching behavior in $RbZnF_3:Tb^{3+}$

(a) Temperature-dependent emission spectra of $RbZnF_3:Tb^{3+}$ sample; (b) Evolution trend of luminescence intensity with increasing temperature

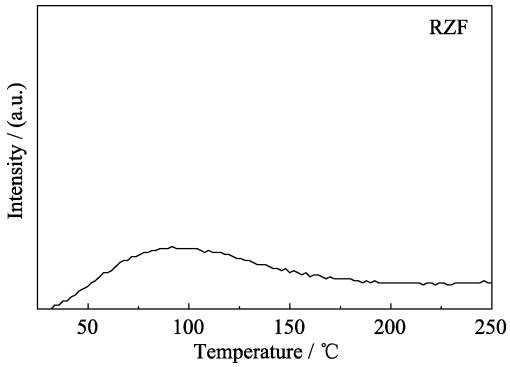

Fig. S7 TL curve of $RbZnF_3$ matrix at different temperatures

Table S1 Variation of cell parameter of $RbZnF_3:0.13Eu^{3+}$ sample with the increase of temperature

Temperature	25 ℃	75 ℃	125 ℃	175 ℃
Space group		Pm3m(221)-Cubic		
a/Å	4.1329	4.1330	4.1369	4.1406
α/(°)	90	90	90	90
V/Å^3	70.5935	70.6140	70.7987	70.9880
R_{wp}	2.67%	2.69%	2.29%	2.33%
R_p	2.11%	2.13%	1.86%	1.89%

References:

[S1] KRESSE G, FURTHMÜLLER J. Efficient iterative schemes for ab initio total-energy calculations using a plane-wave basis set. *Physical Review B*, 1996, **54:** 11169.

[S2] FREYSOLDT C, GRABOWSKI B, HICKEL T, *et al*. First-principles calculations for point defects in solids. *Reviews of Modern Physics*, 2014, **86:** 253.

[S3] ZHANG S B, NORTHRUP J E. Chemical potential dependence of defect formation energies in GaAs: application to Ga self-diffusion. *Physical Review Letters*, 1991, **67:** 2339.